ARTICLE

Check for updates

Isotopic and magnetic proxies are good indicators of millennial-scale variability of the East Asian monsoon

Louise Fuchs[1✉], Jingjing Guo[1], Enno Schefuß[2], Youbin Sun[3], Fei Guo[3], Martin Ziegler[1] & Francien Peterse[1]

Past East Asian Monsoon variability has been reconstructed using oxygen isotopes of cave speleothems as well as proxy indicators from Chinese loess sequences. However, where the speleothem record is dominated by precession cycles, loess magnetic susceptibility primarily shows a glacial-interglacial pattern. Here we generate a ~130,000 years high resolution record of plant wax hydrogen isotopes from a loess section on the western Chinese Loess Plateau that can directly be compared with both speleothem oxygen isotopes and with magnetic susceptibility from the same section. We find that variations in our plant wax hydrogen isotope record follow the precessional pattern of the speleothem record as opposed to the glacial-interglacial changes in magnetic susceptibility. We propose that hydrogen isotopes mainly record precipitation during the growing season, whereas magnetic susceptibility represents an annual climate signal, including precipitation and temperature. Our findings imply that summer vs annual climate variability is driven by distinct orbital forcings.

[1] Department of Earth Sciences, Utrecht University, 3584 CS Utrecht, the Netherlands. [2] MARUM-Center for Marine Environmental Sciences, University of Bremen, D-28334 Bremen, Germany. [3] State Key Laboratory of Loess and Quaternary Geology, Institute of Earth Environment, Chinese Academy of Sciences, Xi'an 710061, China. ✉email: l.fuchs@uu.nl

The East Asian Monsoon (EAM) is one of the world's strongest climate systems and controls the water supply to over one-third of the global population[1]. It is composed of the East Asian Summer Monsoon (EASM) that dominates during interglacial periods and transports moisture and heat from the low-latitude oceans towards northern China, and the East Asian Winter Monsoon (EAWM) that dominates during glacial periods and is characterized by cold, dry Siberian air moving southward[2]. The EASM variability is recorded in the oxygen isotopes ($\delta^{18}O$) of Chinese cave speleothems, where low values reflect periods of a more intense EASM[2–5]. Speleothems from the Hulu and Sanbao caves have provided a high-resolution, well-dated record of EASM variability over the last 640 thousand years (kyr). This record is dominated by a strong precession signal (23 kyr cycle), which has been explained by the EASM strength being mainly driven by Northern Hemisphere (NH) summer insolation[2,3,5]. However, it has also been argued that the changes in the speleothem $\delta^{18}O$ record contain an annual signal or contributions from the Indian Summer Monsoon[6–8], or are rather forced by insolation variations at low-latitudes (30°N-30°S)[9,10], where temperature gradients between land and sea, and between hemispheres drive the position of the Inter-Tropical Convergence Zone (ITCZ) and monsoon rainfall[9,11]. The latter scenario would also explain the absence of a clear signal of NH ice sheet changes in the speleothem records. Regardless, the presence of abrupt variations in the speleothem record coinciding with Heinrich (H) events does indicate an imprint of high-latitude climate dynamics on the EASM on sub-orbital timescales[2,3,5]. Past variation in EASM intensity has also been inferred from many proxy records from Chinese loess sequences, where alternating layers of loess and paleosols represent periods with a dominating winter (glacials) and summer (interglacials) monsoon, respectively[12,13]. The loess layers are characterized by larger grain size (GS) and lower magnetic susceptibility (MagSus), whereas the paleosol layers have smaller GS and higher MagSus. MagSus is traditionally used as a proxy for the intensity of the EASM which delivers ~80% of the precipitation to the Chinese Loess Plateau (CLP), assuming that MagSus increases during pedogenesis under warmer and wetter conditions prevailing during the summer monsoon season[14,15]. Similarly, GS is generally used as a proxy for the strength of the EAWM linked through wind intensity[12].

Interestingly, MagSus records from the CLP show a dominant 100 kyr cycle related to the glacial-interglacial variability, which is not recorded by the speleothem $\delta^{18}O$ records, whereas both proxies are generally interpreted as reflecting EASM variation[1,2,11]. A possible explanation for this discrepancy, known as "the Chinese 100-kyr problem"[16], may be that the archives record slightly different aspects of the EAM climate. Indeed, the exact interpretation of the speleothem $\delta^{18}O$ records is still under debate with different explanations posited for the effects of precipitation amount, moisture composition, moisture source, and pathway[17–22]. In addition, the temperature dependency of calcite/water fractionation of oxygen isotopes can possibly introduce a temperature overprint on the hydroclimate signal[2,23]. In this study, we will follow the interpretation of model outputs suggesting that orbital scale variations in the speleothem $\delta^{18}O$ records primarily reflect changes in moisture transport and precipitation amount[20], summarized as EASM intensity. Similarly, the MagSus can lose sensitivity to changes in precipitation due to changes in the loess deposition rate, where high deposition rates may cause a dilution of the MagSus signal, especially during glacial periods with dominating winter monsoon[24], and low deposition rates, in combination with bioturbation, could smooth out the shorter orbital cycles[25–28]. In addition, MagSus only responds to precipitation when the mean annual precipitation is higher than 200 mm/yr and lower than 2200 mm/yr[29].

MagSus is, next to precipitation, also determined by temperature, as well as soil organic content, carbonate content, type of organic matter and pH[29,30].

Multiple studies have attempted to explain the discrepancy in dominant orbital cycles present in speleothem and loess proxy records. For example, a recent study produced a spliced loess record of MagSus for the interglacials and inversed sand content for the glacials to circumvent the dilution of the MagSus signal during glacials, based on the assumption that variations in EASM strength are then recorded by sand content, determined by the inverse relation of the EASM with the strength of the winter monsoon that delivers this sand to the CLP[27]. Spectral analysis of this record indeed indicated the presence of a dominant 23 kyr cycle, demonstrating that the strong response of EASM to summer insolation is also represented in loess-paleosol records from the CLP. Notably, another study aimed at solving this same discrepancy found a strong 100 kyr cyclicity in their EASM intensity record that they based on the carbon isotopic composition of snail shells ($\delta^{13}C_{shell}$) stored in a loess-paleosol sequence from the central CLP[31]. They assumed a link between $\delta^{13}C_{shell}$ and that of the $\delta^{13}C$ of the vegetation consumed by the snails, which is controlled by local precipitation and thus mainly the EASM[32]. Since snail shells are composed of secondary carbonate, they are, therefore, unaffected by changes in sourcing, pedogenesis, or deposition rate that could alter or smoothen the cyclicities present in the loess record[31]. The dominance of the 100 kyr cycle in that record, as also found in those of loess proxies, thus indicates a primary forcing by NH ice volume rather than local summer insolation. However, earlier studies that used the $\delta^{13}C$ of inorganic carbonate ($\delta^{13}C_{IC}$) to reconstruct EASM intensity for two high-resolution loess sequences in the arid northwestern CLP found that these records contain significant 23-, 41-, and 100 kyr cycles, although the latter is most dominant[33,34]. They linked $\delta^{13}C_{IC}$ with vegetation density, which, on the western CLP, is mainly controlled by precipitation, and thus EASM intensity[35], although changes in the mixing ratio of detrital and pedogenic carbonates may also influence $\delta^{13}C_{IC}$[33]. The same three cycles are also present in the Ca/Ti record from the western CLP, where this ratio was linked to precipitation-induced leaching intensity associated with summer rainfall[36]. The distinct cyclicities in each of these proxy records suggests that they likely reflect different aspects of the EASM, and also record hydrology differently than the $\delta^{18}O$ of speleothems, to which they are compared. Thus, the dominant driver of EASM intensity, as it is recorded in loess-paleosol sequences, remains unclear.

We here aim to solve the orbital discrepancy by using hydrogen isotope compositions of plant waxes ($\delta^{2}H_{wax}$) stored in the Yuanbao section on the western CLP (Fig. 1a) to generate a direct hydrologic record of EASM intensity over the past ~130 kyr. The Yuanbao section is characterized by exceptionally high deposition rates (5 to 143 cm kyr^{-1})[37] that allows the generation of high resolution records that capture millennial scale events. Since previous studies from the modern CLP have shown that temperature and evapo-transpiration have a small impact on soil water $\delta^{2}H$ in non-desert regions where MAP>400mm[38], as is the case in Yuanbao (Fig. 1b) and also shown in the global monsoonal system[39], the $\delta^{2}H_{wax}$ primarily reflects the isotopic composition of meteoric water supplied during plant growth[40,41]. This allows us to make the comparison of EASM proxy behaviour between archives, i.e., $\delta^{2}H_{wax}$ vs. speleothem $\delta^{18}O$, as well as between proxies in the same archive, i.e., $\delta^{2}H_{wax}$ vs. MagSus from the same loess section. Subsequent assessment of the orbital forcings of these proxies should lead to identification of the mechanism(s) resulting in the distinct cyclicities between loess and speleothem-based EASM records.
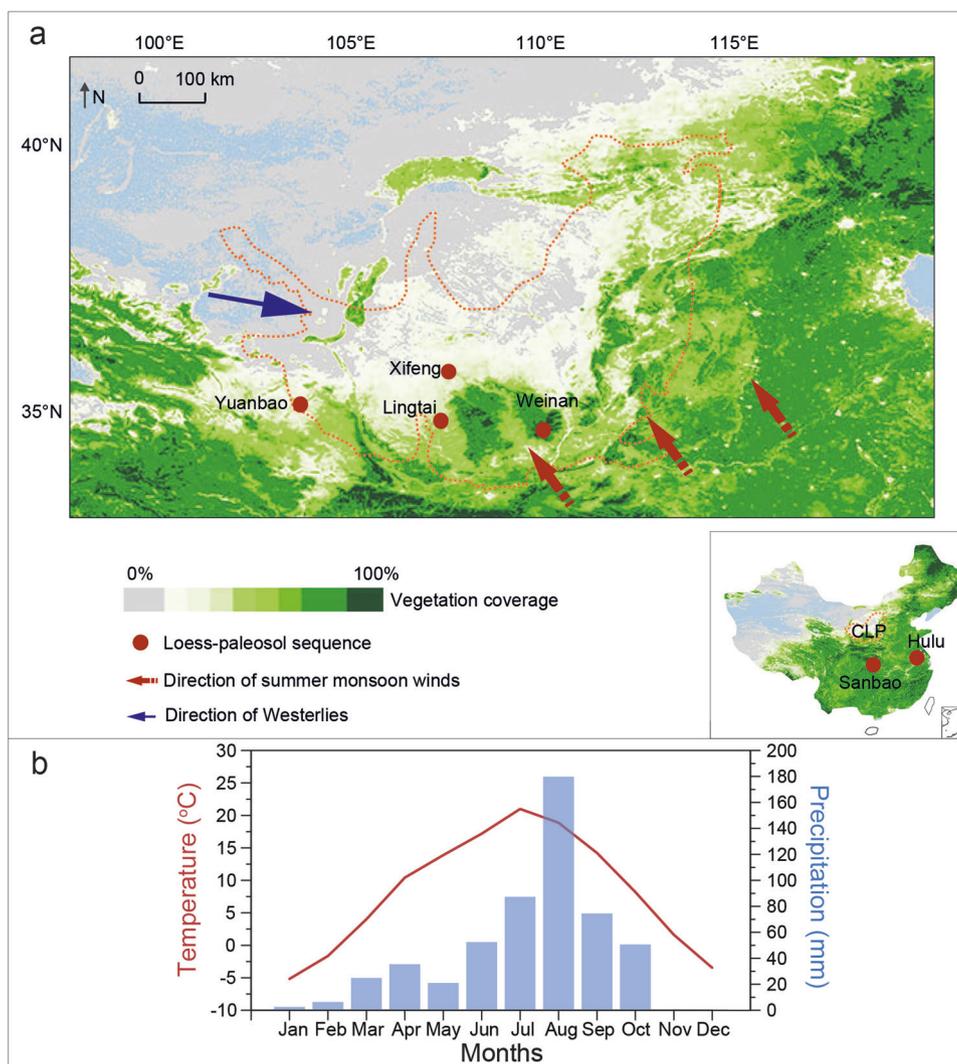
Fig. 1 Map indicating the position of the Chinese Loess Plateau and meteorological data from the area. (**a**) Map (modified from Lu et al., 2019[79]) indicating the position of the Chinese Loess Plateau (CLP), the location of the study site Yuanbao and loess sections cited in the main text, the Hulu and Sanbao caves, and the modern vegetation coverage of the CLP. Red arrows indicate dominant wind directions of the East Asian monsoon system. (**b**) Monthly averaged meteorological data from 2016 to 2017 at Yuanbao: air temperature (red line) and monthly precipitation amount (purple bars) derived from China Meteorological Data Service Center, http://data.cma.cn/en.

Results and discussion

The Yuanbao $\delta^2 H_{wax}$ record. The $\delta^2 H_{wax}$ (compensated for ice-volume induced changes in the global hydrological cycle) ranges from −119‰ to −201‰ (Fig. 2d), where the lowest values occur during interglacial periods and glacial periods are characterized by less negative $\delta^2 H_{wax}$. Since plant waxes are mostly synthesized during the growing season[40,41], the $\delta^2 H_{wax}$ likely represents the isotopic composition of their main water source during this season, i.e., soil moisture[41]. On a global scale, the $\delta^2 H$ of plant source water follows that of (amount weighted average) meteoric water[41]. Given that ~80% of the precipitation at the CLP falls during summer[42], this implies that $\delta^2 H_{wax}$ at Yuanbao reflects the isotopic composition of EASM associated precipitation, and should thus vary according to the same processes which control speleothem $\delta^{18}O$. Hence, variations in the plant wax record presumably reflect a combined effect of upstream depletion, precipitation amount, and atmospheric circulation changes[3,20], where lower $\delta^2 H_{wax}$ values indicate an increased EASM intensity, with more precipitation sourced from the Pacific Ocean, whereas higher $\delta^2 H_{wax}$ values indicate less precipitation, derived from more local sources[3,20]. However, $\delta^2 H_{wax}$ may also be influenced

by vegetation change, as the fractionation of hydrogen isotopes during leaf wax synthesis differs between vegetation types[43]. For example, larger fractionation occurs in grasses than in shrubs[41], and may thus introduce variations in $\delta^2 H_{wax}$ independent of climate. The stable carbon isotopic composition of bulk organic carbon and plant waxes indicates that on part of the CLP, vegetation changed between C_3 and C_4 plant types over glacial-interglacial cycles[44–48]. At Yuanbao, however, the $\delta^{13}C_{wax}$ record only reveals minor scale variation ranging from −30.5‰ to −32.9‰ (Fig. 2e). These values all fall within the range of C_3 plants, likely due to the high elevation of the site (2177 m asl) causing insufficient temperatures for C_4 plants to be favoured[44,45,49]. This indicates that at Yuanbao, changes in $\delta^2 H_{wax}$ are primarily caused by changes in precipitation $\delta^2 H$.

The exceptionally high resolution of our record facilitated by the high deposition rate at Yuanbao reveals millennial scale variations in EASM intensity, in particular during the interval corresponding to Marine Isotope Stage (MIS) 3 (Fig. 2d). The Yuanbao $\delta^2 H_{wax}$ record clearly shows excursions towards more positive values at times that match with H events (H2-H6) similarly recognized in the speleothem record (Fig. 2d, f). The
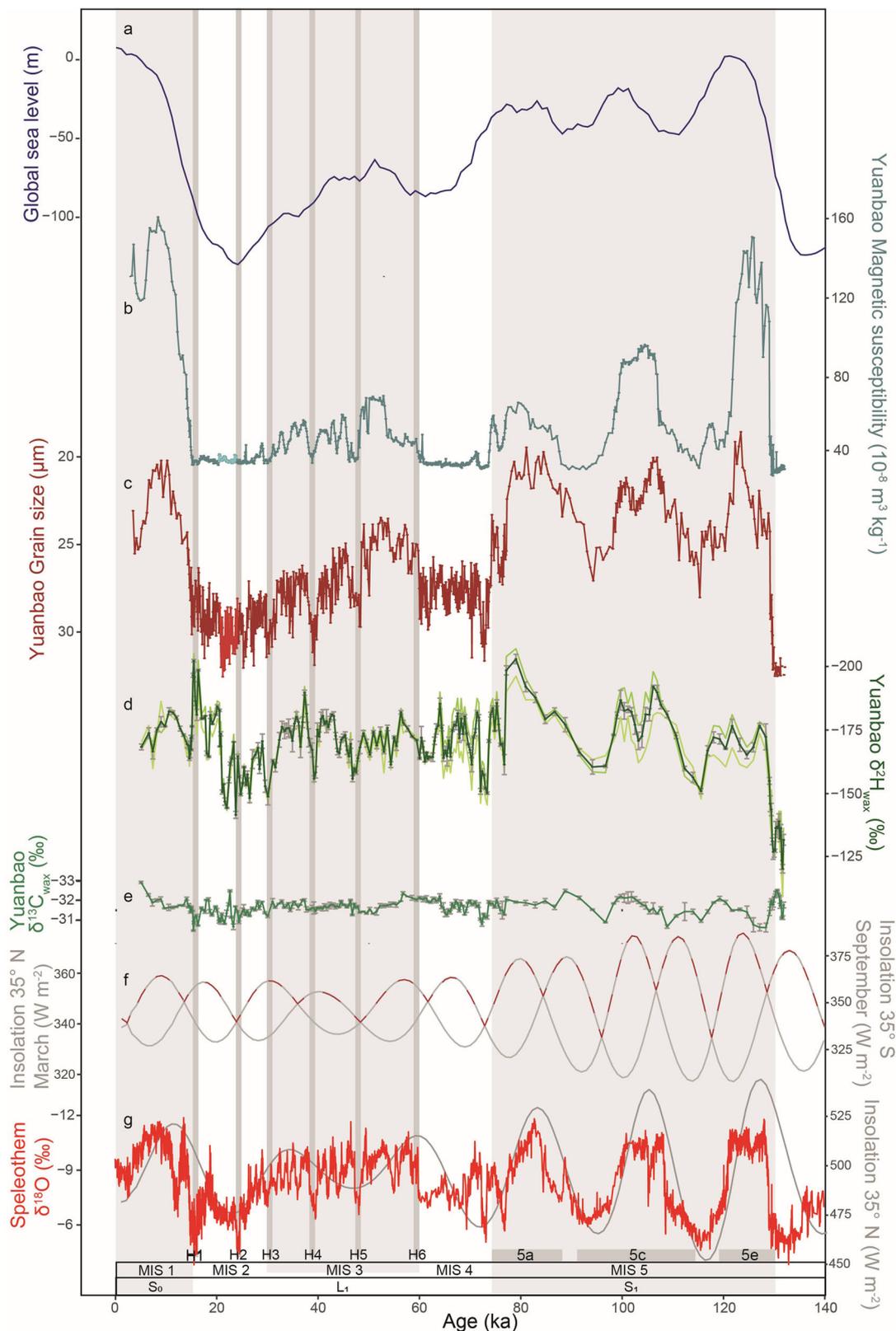
Fig. 2 Comparison of proxy records for the Yuanbao loess section with global climate records. (**a**) Sea level stack[69], (**b**) Magnetic susceptibility, (**c**) Mean grain size, (**d**) Ice-corrected δ^2H_{wax} (dark green; δ^2H_{C31} and δ^2H_{C29} in light and lighter green, respectively). Error bars indicate standard deviation based on at least duplicate analysis. VSMOW – Vienna standard mean ocean water, (**e**) $\delta^{13}C_{wax}$. Error bars indicate standard deviation based on at least duplicate analysis. VPDB – Vienna Peedee belemnite, (**f**) Comparison between insolation and half precession signal between North and South hemisphere (35° N–35° S). The grey lines indicate monthly mean insolation in March and monthly mean insolation in September, the maximum values of these two are in red dashed lines, (**g**) Composite speleothem $\delta^{18}O$ record from the Hulu[2] and Sanbao[5] caves (red), and June 21st insolation at 35°N[80]. Marine Isotope Stages (MIS) and Heinrich events (H) are indicated with grey bars. Alternating loess (L) and paleosol (S) layers are indicated at the bottom of the lower panel.

imprint of these North Atlantic climate events in the Yuanbao record suggests that strengthening of the Westerlies as a result of the slowdown of the AMOC reduced the inland penetration of the EASM during these intervals[12,50,51], and thus blocked the delivery of moisture from remote sources and a more negative isotope signal to the CLP. In addition, the glacial conditions reduced sea surface temperatures and the size of the West Pacific warm pool[52], leading to a weakening of the EASM intensity and making way for polar air from high latitudes to reach the CLP. Notably, these millennial scale events are not resolved in other available $\delta^2 H_{wax}$ records from the CLP (e.g., Weinan[47], Xifeng[53,54], Lingtai[49]; Supplementary Fig. 1), likely due to the lower sedimentation rates on the central and southern CLP, where these sites are located, introducing a smoothing effect on the record[55], or simply by lower sampling resolution. In addition, the trends in the $\delta^2 H_{wax}$ records from Weinan and Lingtai on the southern edge of the central CLP are different from those in the Yuanbao record. This can possibly be attributed to contributions of additional moisture sources and/or local recycling that influenced $\delta^2 H_{wax}$ at these southern sites[47]. Indeed, the trends in $\delta^2 H_{wax}$ recorded at Xifeng that is located further north are more similar to those from Yuanbao, although the resolution of the latter record remains unprecedented.

Comparison of $\delta^2 H_{wax}$ with speleothem $\delta^{18}O$.

The $\delta^2 H_{wax}$ and $\delta^{18}O$ speleothem records presumably record the same aspect of hydroclimate, i.e., the isotopic composition of EASM precipitation driven by changes in moisture transport and precipitation amount[5,40,41,56], and are thus expected to show similar behaviour over time. The two records indeed vary in concert on both precessional and millennial timescales (Figs. 2d, g, 3). The strong similarity between the $\delta^2 H_{wax}$ and speleothem records thus suggests that the main driver of their variability is the same. Assuming that $\delta^2 H_{wax}$ is a growing-season signal, this implies that speleothem $\delta^{18}O$ indeed also represents a summer monsoon signal, as previously suggested based on summer insolation as main driver of the EASM and the fact that the majority of annual precipitation (~80%) falls during summer[2,57–59]. The phase analysis between $\delta^2 H_{wax}$ and $\delta^{18}O$ shows that both records are in phase during MIS 5, but that $\delta^2 H_{wax}$ is leading speleothem $\delta^{18}O$ during MIS 3 (Supplementary Fig. 2). This could be the result of the low insolation forcing during that time, giving way to other factors that may influence precipitation isotopes at Yuanbao, such as high-latitude climate variability (shown by the millennial scale H events), or the distance between the location of the caves and Yuanbao, and possibly the high elevation and the vicinity of Yuanbao to the Tibetan Plateau that can influence the atmospheric teleconnections bringing EASM precipitation inland. Regardless, in line with the similarities between the records, the main periodicity present in the $\delta^2 H_{wax}$ record is precession (23 kyr; Fig. 3). The period from 132-70 ka, corresponding to the last interglacial (MIS 5), also shows half-precessional cycles (Fig. 4), which is something that has so far only been observed in loess proxy records from the Caotan section, also located on the northwestern part of the CLP[60]. The presence of half-precession cycles indicates an influence of low-latitude insolation forcing on the EASM, likely through ocean-atmospheric connections transporting moisture from the West Pacific warm pool to inland China[60], where the sea surface temperature of the West Pacific is highly dependent on both NH and southern hemisphere (SH) summer insolation[61]. The fact that insolation from spring and autumn equinoxes are out of phase by half a precession cycle creates this pattern, as there are two insolation maxima in the tropics during one precession cycle[62]. Half-precessional cycles are also weakly present during 50–20 ka, although they are below the

95% confidence interval. The expression of these cycles during interglacials can be explained by the amplitude of NH and SH insolation (35° N and 35° S, Fig. 2f), which is higher during interglacial periods than during glacial periods[63]. The EASM thus relays low latitude signals from the Pacific to the CLP[60,64,65]. Furthermore, Sun and Huang (2006) noted that the speleothem $\delta^{18}O$ could record changes in moisture from the Pacific to the Indian Ocean, but that the moisture coming from the Indian Ocean does not reach the CLP due to its position relative to the Himalayas, which blocks this moisture transport. Instead, changes in $\delta^2 H_{wax}$ should then show variations in moisture from the South China Sea (related to the Pacific) vs. the West Pacific warm pool (tropical Pacific), indicating the source of the moisture associated with the half-precessional cycles[60].

The relative amplitude of glacial-interglacial variability is minor compared to that in sea level stack and global ice volume records (Fig. 2a). And although the $\delta^2 H_{wax}$ shows a weak 100 kyr cycle (Fig. 3), this is not significant due to the restricted length of the record (~130 kyr). This cyclicity could come from an additional sensitivity to NH ice volume that does not directly impact the speleothem record. The changes in the $\delta^2 H_{wax}$ record are often abrupt and show a sawtooth pattern that is reversed to that in the global benthic stack, i.e., $\delta^2 H_{wax}$ can rapidly become more positive during glacial inceptions, whereas the benthic stack reflects a slow buildup of ice sheets[66] (Fig. 2). Similar rapid changes into glacial periods are present in the Yuanbao GS record, suggesting that they could be linked to the strength of the EAWM, which is closely linked to NH ice volume on orbital timescales[67,68]. The location and high elevation of Yuanbao relative to that of the caves could explain the higher sensitivity of $\delta^2 H_{wax}$ to high-latitude climate forcings compared to that of speleothem $\delta^{18}O$.

Comparison of $\delta^2 H_{wax}$ record with MagSus at Yuanbao.

The generation of a MagSus record for the exact same section as used for $\delta^2 H_{wax}$ analysis allows for a direct comparison of the two records, which are both assumed to reflect EASM intensity. However, the amplitude and trend of the MagSus record for the Yuanbao section are different from that of the $\delta^2 H_{wax}$ record, as well as from the $\delta^{18}O$ speleothem record (Fig. 2b, d, g). The MagSus record clearly follows the pattern of a MIS 5e that is higher than 5c which is again higher than 5a, followed by a subsequent maximum during MIS 1 that is typically also seen in sea level (Fig. 2a, b) and thus the structure of the benthic $\delta^{18}O$ stacked record[69]. This in turn suggests that next to precession, NH ice volume and global climate also exert an influence on the MagSus signal[25].

Indeed, the MagSus record contains the expected 23 kyr cycle, however, the 100 kyr cycle is also prominent in this record (Fig. 3). Although this cycle is not significant due to the length of our record, longer MagSus records from the CLP all contain a prominent 100 kyr signal[1,47,67,70]. The precession signal may be introduced by the influence of NH summer insolation on EASM intensity that is recorded by MagSus specifically in the paleosol layers[27,33]. These layers are presumably well resolved and relatively little impacted by smoothing processes due to the high deposition rates at Yuanbao[37], which facilitates their registration of precession-to-millennial scale EASM intensity signals. Regardless, the MagSus and $\delta^2 H_{wax}$ records show different trends also within the paleosol layers representing interglacials (Fig. 2). Given that $\delta^2 H_{wax}$ mostly records the growing season, any offsets with MagSus are likely introduced during winters, and thus imply that MagSus represents both summer precipitation and annual temperature signals rather than solely EASM intensity[11,16,26]. The contribution of an annual temperature signal, and thus the imprint of the NH ice volume, would then explain the 100 kyr
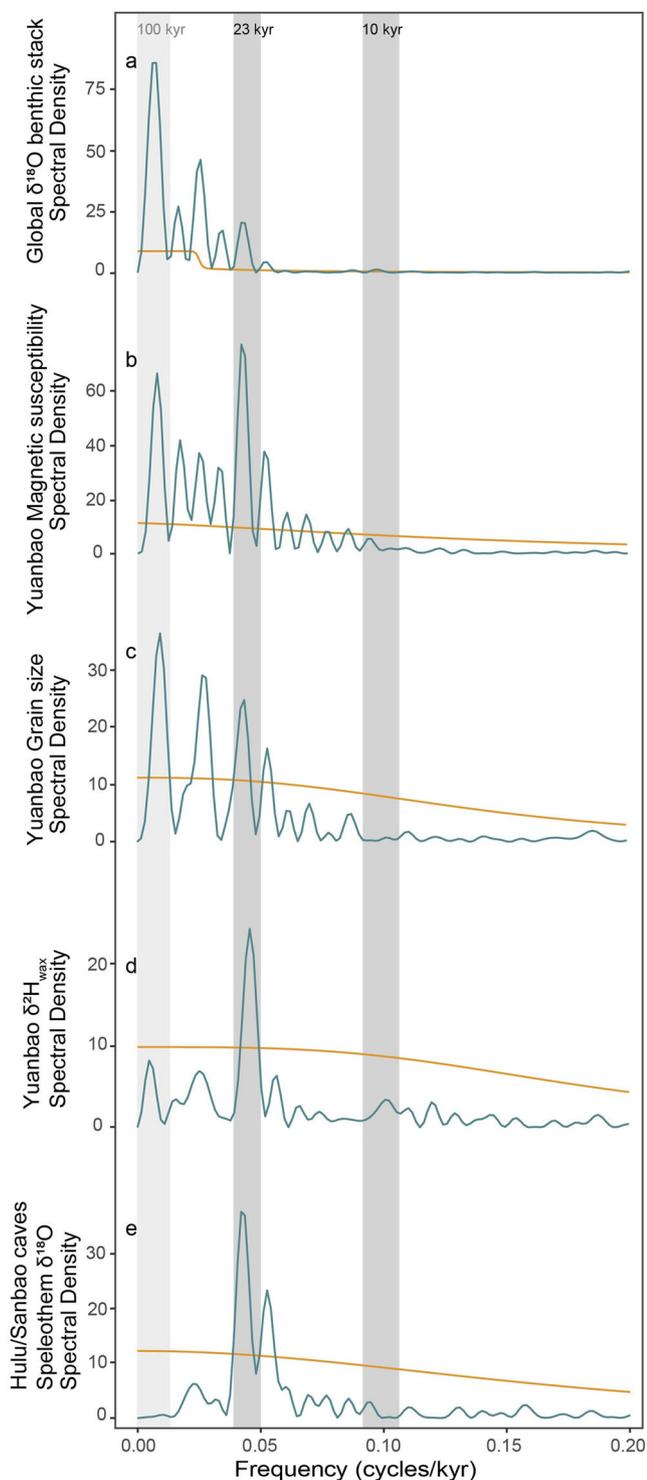
Fig. 3 Spectra of time series of the proxy records for the Yuanbao loess section compared to global climate records. Spectral analysis of (**a**) δ18O benthic stack[69], (**b**) Magnetic susceptibility from Yuanbao (this study), (**c**) Mean grain size from Yuanbao, (**d**) Ice-corrected δ2Hwax from Yuanbao, and (**e**) Hulu/Sanbao speleothem δ18O records[2,5]. Orange lines represent the 99% significance level bending power law (B.P.L.). All spectral analyses for the Yuanbao section, the speleothem δ18O record and the benthic stack span to 132 ka. Vertical bars highlight primary orbital periods of the 23 and 100 kyr cycles. Frequencies <0.025 are not significant due to the length of our record (132 kyr). Half-precessional cycles are recognized by a frequency of ~0.1.

periodicity in the MagSus record. Hence, we suggest that the difference in the MagSus and δ2Hwax records can be explained by the distinct sensitivity of these two proxies to summer precipitation and annual temperature.

Conclusions

Since δ2Hwax is linked to the growing season of the vegetation from which the leaf wax lipids are derived, the similarities between precession-to-millennial scale variabilities of precipitation isotopes recorded by plant waxes in the Yuanbao section of the CLP and those by speleothem δ18O indicate that both records reflect a summer signal, i.e., that of EASM intensity. The dominant 23 kyr cyclicity in both records points to NH summer insolation as their main driver. The additional presence of half-precession cycles in the Yuanbao δ2Hwax record during interglacials indicates that low-latitude insolation forcings reach further north than generally anticipated. In contrast, MagSus recorded in the same loess section and traditionally also assumed to reflect EASM intensity through precipitation-induced pedogenesis, follows the trends and amplitude represented in global sea level, implying a strong control of NH ice volume with a prominent 100 kyr cycle. The different amplitude and periodicities in the MagSus record are thus explained by the contribution of a winter temperature signal, implying that MagSus is recording the effects of both summer precipitation and annual temperature on pedogenesis. The discrepancy in the main cyclicities between the loess proxies and the water isotopes (δ2Hwax and speleothem δ18O) thus has high potential for distinguishing the orbital and glacial imprints on EAM variability for further studies.

Methods

Study site. Yuanbao is situated on the western part of the CLP at 2177 m above sea level (asl; 35.63°N, 103.17°E, Fig. 1a). The mean annual air temperature (MAAT) in Linxia, the closest weather station (35.15°N, 103.63°E)[37], is 7.3 °C[71]. This translates into a MAAT of 5.7 °C at the elevation of the sample site (based on a lapse rate of 0.6 °C 100 m^{-1}) with temperatures of −6.1 °C in winter, and 12.2 °C during the summer growing season (April–October). The mean annual precipitation (MAP) is 500 mm yr^{-1} of which 80% falls between May and September (Fig. 1b)[72]. The Yuanbao section is characterized by exceptionally high deposition rates (5 to 143 cm kyr^{-1})[37] that enabled the generation of high resolution records. Samples from the upper 40 m were collected at 5 cm intervals in August 2019 and stored in geochemical sampling bags for transport to the laboratory in Utrecht, where they were freeze dried and homogenized prior to analysis.

Magnetic susceptibility and grain size analysis. Magnetic susceptibility and grain size were analysed at 5 cm resolution (n = 120) at the Institute of Earth Environment, Chinese Academy of Sciences[37]. Low-frequency mass magnetic susceptibility was measured with a Bartington Instruments MS2 meter. After removal of organic matter (10 ml, 10% H_2O_2) and carbonate (10 ml, 10% HCl), the grain size distributions were determined using a Malvern 2000 laser diffraction instrument. Measurement uncertainty was <10% for magnetic susceptibility and <2% for mean grain size.

Chronology. The upper 40 m of the Yuanbao section covers the past ~132 kyr based on the alignment of GS and MagSus to the quartz GS and MagSus records from the drill core collected at Yuanbao in 2017[37]. The latter GS record was matched with the benthic δ18O record[66], selecting tie points to link the loess (L)/ paleosol (S) boundaries to the glacial/interglacial transitions. This method is commonly accepted to establish age-depth models for
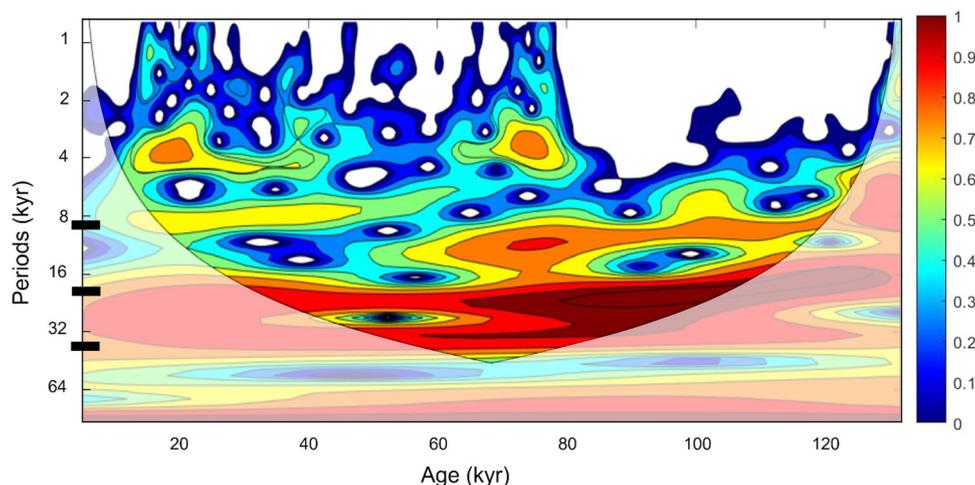
Fig. 4 Wavelet power spectrum of ice-corrected δ^2H_{wax} record from Yuanbao. Warm and cold shadings indicate the power of the correlation. Significant sections are enclosed by contours. Black dashes represent half-precession (10 ka), precession (23 ka) and obliquity (41 ka) cycles, respectively.

loess-paleosol sequences from the CLP[12,33,37]. This age-depth model was supported by optically stimulated luminescence (OSL) dates from a nearby loess-paleosol sequence[73]. In short, the S0/L1, L1/S1, S1/L2 boundaries were linked to the transitions of marine isotope stage (MIS) 1/2 (14 ka), 4/5 (70 ka), 5/6 (132 ka), respectively. Three age control points were additionally chosen to match L1SS1-2 to MIS 3 (27–59 ka). Finally, four additional tie points were added to link H events in the GS and speleothem $\delta^{18}O$ records (Supplementary Fig. 3). This age model was assessed by a phase analysis between Yuanbao GS and speleothem $\delta^{18}O$, showing that both records are in phase (Supplementary Fig. 4).

Lipid biomarker analysis. Long chain n-alkanes were extracted (3x) from ~30 g loess ($n = 251$) with dichloromethane (DCM): MeOH (9:1, v-v) using a MEX microwave extractor. The total lipid extracts (TLEs) were filtered over a paper filter (Whatman grade 42 Ashless Filter Paper, 55 mm diameter), then dried under N_2. Subsequently, TLEs were split into an apolar and polar fraction over an activated Al_2O_3 column eluting with hexane:DCM (9:1, v-v) and DCM:MeOH (1:1, v-v), respectively. An internal standard was added to the apolar fraction, consisting of 64 μL squalane.

The apolar fractions, containing the n-alkanes, were analysed on a Hewlett Packard gas chromatograph (GC) equipped with a CP-sil 5CB fused silica column (30 m, 0.32 mm, 0.10 um) coupled to a flame ionization detector (FID). Helium was used as a carrier gas (1 mL/min at constant flow). The GC oven temperature program was as follows: 70 °C to 130 °C (at 20 °C/min), to 320 °C (at 4 °C/min), at which it was held isothermal for 20 min. The n-alkanes were identified and quantified by using the internal standard, and manual integration of the peak areas using Chemstation software B.04.03.

δ^2H analyses of n-alkanes were conducted on a MAT253 isotope ratio mass spectrometer (Thermo Fisher Scientific) coupled via a GC IsoLink operated at 1420 °C to a GC (TRACE, Thermo Fisher Scientific) equipped with a PTV injector and a HP-5ms column (30 m, 0.25 mm, 1 μm). Each sample was measured at least in duplicate. δ^2H values were calibrated against H_2 reference gas of known isotopic composition and are given in ‰ VSMOW (Vienna Standard Mean Ocean Water). Accuracy and precision were controlled by a lab internal n-alkane standard calibrated against the A4-Mix isotope standard (provided by A. Schimmelmann, University of Indiana) every six measurements and by the daily determination of the H_3^+ factor. Measurement precision was determined by calculating the difference between the analysed values of each standard measurement and the long-term mean of standard measurements, which yielded a 1σ error of 3‰. The analytical reproducibility (1-σ standard deviation) of δ^2H analyses for the n-C_{29} and n-C_{31} alkane was 2 and 3‰ VSMOW on average, respectively, with maximum values of 6 (n-C_{29}) and 5 (n-C_{31}) ‰ VSMOW. H_3^+ factors varied between 4.9 and 5.2 (mean ± s.d., 5.1 ± 0.1). Precision (1-σ standard deviation) of the squalane internal standard was 6‰. $\delta^{13}C$ analyses of n-alkanes were conducted on a MAT252 isotope ratio mass spectrometer (Thermo Fisher Scientific) coupled via a gas chromatograph-combustion (GC-C) interface with a nickel catalyzer operated at 1000 °C to a GC (Trace, Thermo Fisher Scientific) equipped with a PTV injector and a HP-5ms column (30 m, 0.25 mm, 0.25 μm). Each sample was measured at least in duplicate if sufficient material was available. $\delta^{13}C$ values were calibrated against CO_2 reference gas of known isotopic composition and are given in ‰ VPDB (Vienna Pee Dee Belemnite). Accuracy and precision were determined by measuring n-alkane standards calibrated against the A4-Mix isotope standard every six measurements. The difference between the long-term means and the measured standard values yielded a 1σ error of 0.3‰. The analytical reproducibility (1-σ standard deviation) of $\delta^{13}C$ analyses for the n-C_{29} and n-C_{31} alkane was 0.1‰ VSMOW on average with maximum values of 0.5‰ VSMOW for both compounds. For samples with single analysis, the long-term precision was assumed as analytical error. Precision (1-σ standard deviation) of the squalane internal standard was 0.2‰.

From the detected n-alkane distributions and their stable isotopic composition, records of the hydrogen isotopic composition of meteoric water (δ^2H_{wax}), as well as of vegetation change ($\delta^{13}C_{wax}$) were generated based on the weighted mean of the isotopic composition of the most abundant plant waxes (C_{29} and C_{31} n-alkanes). The δ^2H_{wax} record was corrected for ice volume changes which affect isotopes in the global hydrological cycle assuming a Last Glacial Maximum change in global $\delta^{18}O$ of seawater of 1‰ to scale the benthic $\delta^{18}O$ record[74,75] and using the following equation:

$$\delta^2H_{wax\ ice-corrected} = \frac{1000 + \delta^2H_{wax}}{8 \times 0.001 \times \delta^{18}O_{ice} + 1} - 1000 \quad (1)$$

Frequency analysis. Frequency analysis was carried out using Acycle 2.3.1 software[76], using the periodogram function (default settings;

angular frequency of π/4 rad/sample with additive N (0,1) white noise). The wavelet analysis was also conducted under Acycle 2.3.1[77] with the following parameters: period range from 1 to 100, pad = 1, discrete scale spacing = 0.1, Mother = Morlet. All analysed records were standardized and detrended (rLOWESS; Locally Weighted Scatterplot Smoothing). Cross-spectral analyses were performed with the Blackman-Tukey approach using arand-master software after interpolation to a constant time step of 1 ka. Cross-spectral results are also obtained between precession, ice volume, GHG and East Asian monsoon proxies. The coherency spectra of East Asian monsoon proxies with ice volume, GHG and precession are compared with the 80% non-zero coherency level, implying different roles of ice volume, summer insolation and GHG forcing on four proxy records. The following parameters were used to optimize bias/variance properties of spectrum estimates: number of lags = 40 (~1/3 length of record) and samples per analysis = 120. The phase analysis (wavelet coherence; WTC) was performed in a Monte Carlo framework ($n = 1000$)[78], using the MATLAB code available at http://grinsted.github.io/wavelet-coherence/. The WTC helps to detect the period in different frequency bands where the two time series co-vary (but does not necessarily have high power). The black arrows in the figures represent the phase relationship between the two time sequences with rightward, upward and downward arrows indicating in phase, leading phase and lagging phase, respectively. The color scale indicates the amplitude correlations between the two datasets[36].

Data availibility

References

1. An, Z. et al. Global monsoon dynamics and climate change. *Annu. Rev. Earth Planet. Sci.* **43**, 29–77 (2015).
2. Wang, Y. J. et al. A high-resolution absolute-dated late pleistocene monsoon record from Hulu Cave, China. *Science* **294**, 2345–2348 (2001).
3. Cheng, H. et al. The Asian monsoon over the past 640,000 years and ice age terminations. *Nature* **534**, 640–646 (2016).
4. Liu, Z. et al. Chinese cave records and the East Asia Summer Monsoon. *Quat. Sci. Rev.* **83**, 115–128 (2014).
5. Wang, Y. et al. Millennial- and orbital-scale changes in the East Asian monsoon over the past 224,000 years. *Nature* **451**, 1090–1093 (2008).
6. Caley, T., Roche, D. M. & Renssen, H. Orbital Asian summer monsoon dynamics revealed using an isotope-enabled global climate model. *Nat. Commun.* **5**, 5371 (2014).
7. Clemens, S. C., Prell, W. L. & Sun, Y. Orbital-scale timing and mechanisms driving Late Pleistocene Indo-Asian summer monsoons: Reinterpreting cave speleothem δ18O. *Paleoceanography* **25**, PA4207 https://doi.org/10.1029/2010PA001926 (2010).
8. Baker, A. J., Mattey, D. P. & Baldini, J. U. L. Reconstructing modern stalagmite growth from cave monitoring, local meteorology, and experimental measurements of dripwater films. *Earth Planet. Sci. Lett.* **392**, 239–249 (2014).
9. Kutzbach, J. E. Monsoon climate of the early holocene: climate experiment with the Earth's orbital parameters for 9000 years ago. *Science* **214**, 59–61 (1981).
10. Beck, J. W. et al. A 550,000-year record of East Asian monsoon rainfall from 10Be in loess. *Science* **360**, 877–881 (2018).
11. Cheng, H. et al. Milankovitch theory and monsoon. *Innovation* **3**, 100338 (2022).
12. Porter, S. C. & An, Z. Correlation between climate events in the North Atlantic and China during the last glaciation. *Nature* **375**, 305–308 (1995).
13. An, Z. et al. Asynchronous Holocene optimum of the East Asian monsoon. *Quat. Sci. Rev.* **19**, 743–762 (2000).
14. An, Z., Kukla, G. J., Porter, S. C. & Xiao, J. Magnetic susceptibility evidence of monsoon variation on the Loess Plateau of central China during the last 130,000 years. *Quat. Res.* **36**, 29–36 (1991).
15. Maher, B. A. & Thompson, R. Mineral magnetic record of the Chinese loess and paleosols. *Geology* **19**, 3–6 (1991).
16. Cheng, H. et al. Orbital-scale Asian summer monsoon variations: paradox and exploration. *Sci. China Earth Sci.* **64**, 529–544 (2021).
17. Maher, B. A. & Thompson, R. Oxygen isotopes from Chinese caves: records not of monsoon rainfall but of circulation regime. *J. Quat. Sci.* **27**, 615–624 (2012).
18. Pausata, F. S. R., Battisti, D. S., Nisancioglu, K. H. & Bitz, C. M. Chinese stalagmite δ18O controlled by changes in the Indian monsoon during a simulated Heinrich event. *Nat. Geosci.* **4**, 474–480 (2011).
19. Gebregiorgis, D. et al. A brief commentary on the interpretation of Chinese Speleothem δ18O records as Summer Monsoon intensity tracers. *Quaternary* **3**, 7 (2020).
20. Hu, J., Emile-Geay, J., Tabor, C., Nusbaumer, J. & Partin, J. Deciphering oxygen isotope records from Chinese Speleothems with an isotope-enabled climate model. *Paleoceanogr. Paleoclimatology* **34**, 2098–2112 (2019).
21. Zhang et al. The Asian Summer Monsoon: teleconnections and forcing mechanisms—a review from Chinese Speleothem δ18O records. *Quaternary* **2**, 26 (2019).
22. Zhang, H., Cheng, H., Baker, J. & Kathayat, G. Response to comments by Daniel Gebregiorgis et al. "A brief commentary on the interpretation of Chinese Speleothem δ18O records as Summer Monsoon intensity tracers". *Quaternary* **3**, 8 (2020).
23. Friedman, I. & O'Neil, J. R. Compilation of stable isotope fractionation factors of geochemical interest (Report No. 440KK), Professional Paper. https://doi.org/10.3133/pp440KK (1977).
24. Sun, Y. et al. East Asian monsoon variability over the last seven glacial cycles recorded by a loess sequence from the northwestern Chinese Loess Plateau: East Asian Monsoon Variability. *Geochem. Geophys. Geosyst.* **7**, Q12Q02 https://doi.org/10.1029/2006GC001287 (2006).
25. Lu, H., Zhang, F., Liu, X. & Duce, R. A. Periodicities of palaeoclimatic variations recorded by loess-paleosol sequences in China. *Quat. Sci. Rev.* **23**, 1891–1900 (2004).
26. Nie, J., King, J. W. & Fang, X. Tibetan uplift intensified the 400 k.y. signal in paleoclimate records at 4 Ma. *Geol. Soc. Am. Bullet.* **120**, 1338–1344 (2008).
27. Guo, B. et al. Dominant precessional forcing of the East Asian summer monsoon since 260 ka. *Geology.* https://doi.org/10.1130/G50206.1 (2022).
28. Ma, L., Li, Y., Liu, X. & Sun, Y. Registration of precession signal in the last interglacial paleosol (S1) on the Chinese Loess Plateau. *Geochem. Geophys. Geosyst.* **18**, 3964–3975 (2017).
29. Balsam, W. L. et al. Magnetic susceptibility as a proxy for rainfall: worldwide data from tropical and temperate climate. *Quat. Sci. Rev.* **30**, 2732–2744 (2011).
30. Jenny, H. *Factors of Soil Formation*. (McGraw-Hill, New York, 1941).
31. Bao, R. et al. 100 k.y. pacing of the East Asian summer monsoon over the past five glacial cycles inferred from land snails. *Geology* https://doi.org/10.1130/G50243.1 (2023).
32. Bao, R. et al. Stable carbon and oxygen isotopic composition of modern land snails along a precipitation gradient in the mid-latitude East Asian monsoon region of China. *Palaeogeogr. Palaeoclimatology Palaeoecol.* **533**, 109236 (2019).
33. Sun, Y. et al. Astronomical and glacial forcing of East Asian summer monsoon variability. *Quat. Sci. Rev.* **115**, 132–142 (2015).
34. Sun, Y. et al. Diverse manifestations of the mid-Pleistocene climate transition. *Nat Commun* **10**, 352 (2019).
35. Liu, W., Yang, H., Sun, Y. & Wang, X. δ13C values of loess total carbonate: a sensitive proxy for Asian summer monsoon in arid northwestern margin of the Chinese loess plateau. *Chem. Geol.* **284**, 317–322 (2011).
36. Guo, F. et al. Greenhouse gases modulate the strength of millennial-scale subtropical rainfall, consistent with future predictions. *Clim. Past* **18**, 1675–1684 (2022).
37. Guo, F. et al. Monsoon variations inferred from high-resolution geochemical records of the Linxia loess/paleosol sequence, western Chinese Loess Plateau. *CATENA* **198**, 105019 (2021).
38. Liu, W. et al. Hydrogen isotopic compositions along a precipitation gradient of Chinese Loess Plateau: critical roles of precipitation/evaporation and vegetation change as controls for leaf wax δD. *Chem. Geol.* **528**, 119278 (2019).
39. Niedermeyer, E. M. et al. The stable hydrogen isotopic composition of sedimentary plant waxes as quantitative proxy for rainfall in the West African Sahel. *Geochim. Cosmochim. Acta* **184**, 55–70 (2016).
40. Sessions, A. L., Burgoyne, T. W., Schimmelmann, A. & Hayes, J. M. Fractionation of hydrogen isotopes in lipid biosynthesis. *Organic Geochem.* **30**, 1193–1200 (1999).
41. Sachse, D. et al. Molecular paleohydrology: interpreting the hydrogen-isotopic composition of lipid biomarkers from photosynthesizing organisms. *Annu. Rev. Earth Planet. Sci.* **40**, 221–249 (2012).
42. Liu, W. et al. δ13C variation of C3 and C4 plants across an Asian monsoon rainfall gradient in arid northwestern China. *Glob Change Biol.* **11**, 1094–1100 (2005).
43. Liu, J. et al. Controls on leaf water hydrogen and oxygen isotopes: a local investigation across seasons and altitude. *Hydrol. Earth Syst. Sci.* **27**, 599–612 (2023).

44. Zhang, Z., Zhao, M., Lu, H. & Faiia, A. M. Lower temperature as the main cause of C_4 plant declines during the glacial periods on the Chinese Loess Plateau. *Earth Planet. Sci. Lett.* **214**, 467–481 (2003).

45. Liu, W. et al. Summer monsoon intensity controls C_4/C_3 plant abundance during the last 35 ka in the Chinese Loess Plateau: Carbon isotope evidence from bulk organic matter and individual leaf waxes. *Palaeogeogr. Palaeoclimatology Palaeoecol.* **220**, 243–254 (2005).

46. Zhang, Z., Zhao, M., Eglinton, G., Lu, H. & Huang, C. Leaf wax lipids as paleovegetational and paleoenvironmental proxies for the Chinese Loess Plateau over the last 170kyr. *Quat. Sci. Rev.* **25**, 575–594 (2006).

47. Thomas, E. K. et al. Heterodynes dominate precipitation isotopes in the East Asian monsoon region, reflecting interaction of multiple climate factors. *Earth Planet. Sci. Lett.* **455**, 196–206 (2016).

48. Zhou, B., Wali, G., Peterse, F. & Bird, M. I. Organic carbon isotope and molecular fossil records of vegetation evolution in central Loess Plateau since 450 kyr. *Sci. China Earth Sci.* **59**, 1206–1215 (2016).

49. Fuchs, L. et al. Multiproxy records of temperature, precipitation and vegetation on the central Chinese Loess Plateau over the past 200,000 years. *Quat. Sci. Rev.* **288**, 107579 (2022).

50. An, Z. et al. Interplay between the Westerlies and Asian monsoon recorded in Lake Qinghai sediments since 32 ka. *Sci. Rep.* **2**, 619 (2012).

51. Fan, Y., Jia, J., Xia, D., Meadows, M. & Wang, Z. Seasonality of response to millennial-scale climate events of the last glacial: evidence from loess records over mid-latitude Asia. *Geochem. Geophys. Geosyst.* **22**, e2021GC009903 https://doi.org/10.1029/2021GC009903 (2021).

52. Wang, P. Response of Western Pacific marginal seas to glacial cycles: paleoceanographic and sedimentological features. *Mar. Geol.* **156**, 5–39 (1999).

53. Liu, W. & Huang, Y. Compound specific D/H ratios and molecular distributions of higher plant leaf waxes as novel paleoenvironmental indicators in the Chinese Loess Plateau. *Organic Geochem.* **36**, 851–860 (2005).

54. Wang, J., Liu, W. & Wang, H. New chronology of the Chinese loess-paleosol sequence by leaf wax δD records during the past 800 k.y. *Geology* **49**, 847–850 (2021).

55. Sun, Y., Wang, X., Liu, Q. & Clemens, S. C. Impacts of post-depositional processes on rapid monsoon signals recorded by the last glacial loess deposits of northern China. *Earth Planet. Sci. Lett.* **289**, 171–179 (2010).

56. Cheng, H., Sinha, A., Wang, X., Cruz, F. W. & Edwards, R. L. The Global Paleomonsoon as seen through speleothem records from Asia and the Americas. *Clim. Dyn.* **39**, 1045–1062 (2012).

57. Cheng, H. et al. A penultimate glacial monsoon record from Hulu Cave and two-phase glacial terminations. *Geology* **34**, 217 (2006).

58. Cheng, H. et al. Ice Age Terminations. *Science* **326**, 248–252 (2009).

59. Chen, J. et al. On the timing of the East Asian summer monsoon maximum during the Holocene—does the speleothem oxygen isotope record reflect monsoon rainfall variability? *Sci. China Earth Sci.* **59**, 2328–2338 (2016).

60. Sun, J. & Huang, X. Half-precessional cycles recorded in Chinese loess: response to low-latitude insolation forcing during the Last Interglaciation. *Quat. Sci. Rev.* **25**, 1065–1072 (2006).

61. Terada, K. & Hanzawa, M. Climate of the North Pacific Ocean. *Clim. Oceans* **15**, 431–477 (1984).

62. Berger, A. & Loutre, M. F. Intertropical latitudes and precessional and half-precessional cycles. *Science* **278**, 1476–1478 (1997).

63. Su, Q., Lyu, A., Wu, Z. & Yin, Q. Diverse response of global terrestrial vegetation to astronomical forcing and CO_2 during the MIS-11 and MIS-13 interglacials. *Clim. Dyn.* **60**, 375–392 (2023).

64. Short, D. A., Mengel, J. G., Crowley, T. J., Hyde, W. T. & North, G. R. Filtering of Milankovitch Cycles by Earth's Geography. *Quat. Res.* **35**, 157–173 (1991).

65. Crowley, T. J., Kim, K.-Y., Mengel, J. G. & Short, D. A. Modeling 100,000-year climate fluctuations in pre-pleistocene time series. *Science* **255**, 705–707 (1992).

66. Lisiecki, L. E. & Raymo, M. E. A Pliocene-Pleistocene stack of 57 globally distributed benthic δ18O records: Pliocene-Pleistocene benthic stack. *Paleoceanography* **20**, PA1003 https://doi.org/10.1029/2004PA001071 (2005).

67. Ding, Z. et al. Ice-volume forcing of East Asian Winter Monsoon variations in the past 800,000 years. *Quat. Res.* **44**, 149–159 (1995).

68. Sun, Y., Clemens, S. C., An, Z. & Yu, Z. Astronomical timescale and palaeoclimatic implication of stacked 3.6-Myr monsoon records from the Chinese Loess Plateau. *Quat. Sci. Rev.* **25**, 33–48 (2006).

69. Spratt, R. M. & Lisiecki, L. E. A Late Pleistocene sea level stack. *Clim. Past* **12**, 1079–1092 (2016).

70. Liu, T., Ding, Z. & Rutter, N. Comparison of Milankovitch periods between continental loess and deep sea records over the last 2.5 Ma. *Quat. Sci. Rev.* **18**, 1205–1212 (1999).

71. China Meteorological Administration. http://www.cma.gov.cn.

72. Rao, Z. et al. High-resolution summer precipitation variations in the western Chinese Loess Plateau during the last glacial. *Sci. Rep.* **3**, 2785 (2013).

73. Lai, Z.-P. & Wintle, A. G. Locating the boundary between the Pleistocene and the Holocene in Chinese loess using luminescence. *Holocene* **16**, 893–899 (2006).

74. Fairbanks, R. G., Charles, C. D. & Wright, J. D. Origin of Global Meltwater Pulses. in *Radiocarbon After Four Decades* (eds. Taylor, R. E., Long, A. & Kra, R. S.) 473–500 (Springer New York, 1992). https://doi.org/10.1007/978-1-4757-4249-7_30.

75. Tierney, J. E. & deMenocal, P. B. Abrupt shifts in Horn of Africa Hydroclimate since the last glacial maximum. *Science* **342**, 843–846 (2013).

76. Li, M., Hinnov, L. & Kump, L. Acycle: time-series analysis software for paleoclimate research and education. *Comput. Geosci.* **127**, 12–22 (2019).

77. Torrence, C. & Compo, G. P. A practical guide to wavelet analysis. *Bull. Amer. Meteor. Soc.* **79**, 61–78 (1998).

78. Grinsted, A., Moore, J. C. & Jevrejeva, S. Application of the cross wavelet transform and wavelet coherence to geophysical time series. *Nonlin. Processes Geophys.* **11**, 561–566 (2004).

79. Lu, H. et al. 800-kyr land temperature variations modulated by vegetation changes on Chinese Loess Plateau. *Nat. Commun.* **10**, 1–10 (2019).

80. Laskar, J. et al. A long-term numerical solution for the insolation quantities of the Earth. *A&A* **428**, 261–285 (2004).

Acknowledgements

Author contributions

F.P. designed the research. F.P., F.G. and Y.S. conducted field work, Y.S. provided the magnetic susceptibility and grain size data, L.F. and J.G. extracted and analysed the plant waxes, E.S. generated the isotope data. F.G. conducted the phase analysis of the data. L.F. wrote the manuscript under the supervision of F.P. and M.Z. All co-authors contributed to the discussion of results and the manuscript draft.

Competing interests

The authors declare no competing interests.

Additional information

Supplementary information The online version contains supplementary material available at https://doi.org/10.1038/s43247-023-01090-z.

Correspondence and requests for materials should be addressed to Louise Fuchs.

Peer review information *Communications Earth & Environment* thanks the anonymous reviewers for their contribution to the peer review of this work. Primary Handling Editors: Yama Dixit and Aliénor Lavergne. A peer review file is available.

Reprints and permission information is available at http://www.nature.com/reprints

Publisher's note Springer Nature remains neutral with regard to jurisdictional claims in published maps and institutional affiliations.